catalysts

MDPI

Article

Metal–Organic Framework-Derived Rare Earth Metal (Ce-N-C)-Based Catalyst for Oxygen Reduction Reactions in Dual-Chamber Microbial Fuel Cells

Shaik Ashmath [1], Hao Wu [1], Shaik Gouse Peera [1,2,*] and Tae-Gwan Lee [1,*]

[1] Department of Environmental Engineering, Keimyung University, 1095, Dalseo-gu, Daegu 42601, Republic of Korea; shaikashmath2@gmail.com (S.A.); wuhaobobi@gmail.com (H.W.)
[2] Natural Science Research Institute, Keimyung University, 1095, Dalseo-gu, Daegu 42601, Republic of Korea
* Correspondence: gouse@kmu.ac.kr (S.G.P.); wateree@kmu.ac.kr (T.-G.L.); Tel.: +82-053-580-5601 (S.G.P.)

Abstract: Pt supported on carbon (Pt/C) is deemed as the state-of-the-art catalyst towards oxygen reduction reactions (ORRs) in chemical and biological fuel cells. However, due to the high cost and scarcity of Pt, researchers have focused on the development of Earth-abundant non-precious metal catalysts, hoping to replace the traditional Pt/C catalyst and successfully commercialize the chemical and biological fuel cells. In this regard, electrocatalysts made of transition metals emerged as excellent candidates for ORRs, especially the electrocatalysts made of Fe and Co in combination with N-doped carbons, which produce potentially active M-N_4-C (M=Co, Fe) ORR sites. At present, however, the transition metal-based catalysts are popular; recently, electrocatalysts made of rare earth metals are emerging as efficient catalysts, due to the fact that rare earth metals also have the potential to form rare earth metal-N_4-C active sites, just like transition metal Fe-N_4-C/Co-N_4-C. In addition, mixed valance states and uniqueness of *f*-orbitals of the rare earth metals are believed to improve the redox properties of the catalyst that helps in enhancing ORR activity. Among the rare earth metals, Ce is the most interesting element that can be explored as an ORR electrocatalyst in combination with the N-doped carbon. Unique *f*-orbitals of Ce can induce distinctive electronic behavior to the catalyst that helps to form stable coordination structures with N-doped carbons, in addition to its excellent ability to scavenge the $OH^{\bullet}$ produced during ORRs, therefore helping in catalyst stability. In this study, we have synthesized Ce/N-C catalysts by a metal–organic framework and pyrolysis strategy. The ORR activity of Ce/N-C catalysts has been optimized by systematically increasing the Ce content and performing RDE studies in 0.1 M $HClO_4$ electrolyte. The Ce/N-C catalyst has been characterized systematically by both physicochemical and electrochemical characterizations. The optimized Ce/N-C-3 catalyst exhibited a half-wave potential of 0.68 V vs. RHE. In addition, the Ce/N-C-3 catalyst also delivered acceptable stability with a loss of 70 mV in its half-wave potential when compared to 110 mV loss for Pt/C (10 wt.%) catalyst, after 5000 potential cycles. When Ce/N-C-3 is used as a cathode catalyst in dual-chamber microbial fuel cells, it delivered a volumetric power density of ~300 mW m^{-3}, along with an organic matter degradation of 74% after continuous operation of DCMFCs for 30 days.

Keywords: oxygen reduction reaction (ORR); microbial fuel cells (MFCs); rare earth metal catalyst; Ce-N_4-C active sites; TOC; organic pollutant degradation; volumetric power density

Citation: Ashmath, S.; Wu, H.; Peera, S.G.; Lee, T.-G. Metal–Organic Framework-Derived Rare Earth Metal (Ce-N-C)-Based Catalyst for Oxygen Reduction Reactions in Dual-Chamber Microbial Fuel Cells. *Catalysts* **2024**, *14*, 506. https://doi.org/10.3390/catal14080506

Academic Editors: Loreta Tamasauskaite-Tamasiunaite and Virginija Kepeniene

Received: 26 June 2024
Revised: 15 July 2024
Accepted: 27 July 2024
Published: 5 August 2024

1. Introduction

Water pollution has become a serious threat to the growing human population and high demand for fresh water further worsens the situation [1]. In order to meet the demands for the fresh water to the human community, polluted water is recycled through an extensive process at wastewater treatment plants, which could play a key role in maintaining water quality by removing pathogens and toxic substances, which also include organic contaminants [2]. The secondary treatment, also known as biological wastewater treatment,

especially, helps in degrading the dissolved and suspended organic matter in which microorganisms such as bacteria oxidize the organic matter by biological aerobic oxidation into CO_2 and H_2O [3,4]. The secondary treatment thus involves intensive aeration of the wastewater to promote the growth and oxidation of organic matter from the wastewater. Though biological oxidation is a commonly applied process, it requires high energy input, produces large amounts of sludge, and most importantly, the energy trapped in the organic matter is simply lost during the oxidation of the organic matter [5]. Concerning this process, the application of microbial fuel cells (MFCs) has been attracting significant interest as a simultaneous technology for treating wastewater and generating useful amount of electricity [6,7]. MFCs generate electricity by combined biological and electrochemical reactions that occur in the anodes and cathodes. In the anode, the electrogenic bacteria oxidize the organic matter; as a result, it generates the electrons and protons; the electrons travel through the external electrical circuit, whereas the protons travel through the proton exchange membrane and reach the cathode [8,9]. In the cathode, the electrocatalyst is typically made of metal nanoparticles supported on the carbon, which combines the protons and electrons with the O_2 present in the atmosphere into H_2O, as shown in Equation [10]. The following equations are shown with glucose as a simple organic compound and O_2 as the oxidant.

$$\text{Anodic reaction: } C_6H_{12}O_6 + 6H_2O \rightarrow 6CO_2 + 24H^+ + 24e^- \quad E^o = 0.014 \text{ V vs. RHE} \quad (1)$$

$$\text{Cathode reaction: } O_2 + 4H^+ + 4e^- \rightarrow 2H_2O \quad E^o = 1.23 \text{ V vs. RHE} \quad (2)$$

The efficiency of microbial fuel cells depends on various factors such as indigenous microbial species in the wastewater and the effective formation of biofilm on the anode surface, which strongly influence the electron transfer from the bacterial surface to the anode-conductive electrode. This creates a synergistic microbial community that increases organic matter degradation, depending on the types of organic matter present in the wastewater and their concentrations [11]. In addition to these, electrode materials also play an important role in determining the efficiency of MFCs, both in power output and organic matter degradation [12]. The anode electrode acts as a substrate for the biofilm formation on which bacteria grow. The anode electrode should have the following features: sufficient conductivity to extract electrons from the bacterial surface and transport these electrons to the anode, possess a large surface area, exhibit biocompatibility for the bacterial cells to adhere and form a biofilm, and resist corrosion [13]. The most common types of anodes used in MFCs are carbon cloth/felt/paper/brush type. On the other hand, the cathode electrode on which the oxygen reduction reactor (ORR) occurs contributes to the overall efficiency of the MFCs. The cathode electrode functions by combining the protons and electrons with O_2 in the air to form H_2O, which facilitates in maintaining the electron flow continuously through the external circuit, thus generating the power [14].

The cathode electrode is an essential part of the MFCs which enhances the sluggish ORR with the help of electrocatalysts, which function in reducing the activation energy required for the ORR, thus improving the MFC performance. In general, platinum supported on carbon (Pt/C) is considered as the state-of-the-art catalyst due to the fact that Pt nanoparticles reduce the activation energy required for the ORR, and due to high exchange current density, lower the overpotential for the ORR, thus enhancing the ORR kinetics, in addition to the Pt nanoparticle's ability to reduce the O_2 by a direct 4-electron reduction pathway [15]. Despite the advantages, the commercial applicability of MFCs is hindered by the high cost, scarcity, and poor stability of the Pt/C catalysts. In addition, the Pt/C catalysts also suffer from poisoning in the presence of sulfur, chlorine, and CO compounds [16]. Consequently, scientists are looking for catalysts that are abundant on Earth, exhibit a high ORR activity level, and are inexpensive.

Recently, transition metal-based catalysts of Co and Fe, especially, in combination with N-doped carbons, have attracted considerable interest, as a promising alternative catalyst to the traditional Pt/C catalyst [17]. These transition metal-based catalysts possess several

advantages, such as high catalytic activity toward ORRs, low cost, and superior stability. It is well documented that the transition metal catalysts, Fe and Co, possess active sites composed of Fe-N_4-C/Co-N_4-C, which mimic the active sites of Pt/C catalyst in reducing the O_2 to H_2O with a dominant, direct 4-electron reduction pathway [18]. In addition, the strong coordination bonding between N and transition metals such as Fe and Co also imparts greater chemical stabilities and corrosion resistance for the typical operating potentials and pH of the MFCs [19]. Further, N-doping of the carbon guarantees the high electronic conductivity of the carbon support, which helps in efficient supply of electrons to the Fe-N_4-C/Co-N_4-C active sites. The synergistic effects of N-doped carbons, which also assist in ORRs, and Fe-N_4-C/Co-N_4-C active sites in the catalysts, provide the maximum positive effect on the overall ORR kinetics and are thus classified currently as the best alternative ORR catalyst to the traditional Pt/C catalyst [20]. Several researchers identified Fe-N_4-C/Co-N_4-C catalyst synthesized by a variety of chemical strategies and evaluated their ORR kinetics in acidic/alkaline electrodes, finding that the Fe-N_4-C/Co-N_4-C catalyst delivered similar or even higher ORR activity and stabilities [21,22]. Though transition metal-based catalysts are popular, electrocatalysts made of rare earth metals have recently emerged as efficient catalysts, due to the fact that rare earth metals also have the potential to form rare earth metal-N_4-C active sites, just like transition metal Fe-N_4-C/Co-N_4-C [23]. In addition, the mixed valence states of the rare earth metals could enhance the redox properties that augment ORR activity. In addition, rare earth metal-based catalysts have tremendous electrocatalytic potential due to the localization and incomplete filling of 4*f* electrons [24]. Rare earth metals also form strong bonds with the N and carbon matrix, and this enhances the stability of the electrocatalysts. Moreover, the term rare earth metal often leads to misconceptions. In contrast, rare earth metals are abundant in the Earth's crust when compared to transition and noble metals, particularly metals such as La, Nd, and Ce, which are the most abundant elements of the rare earth metals category [25]. Among these metals, Ce is the most interesting element that can be explored as an ORR electrocatalyst in combination with the N-doped carbon.

Cerium (Ce) is exceptionally interesting due to the fact that Ce exhibits excellent redox properties with its unique shifting in oxidation state from Ce^{3+} to Ce^{4+}, which helps in electron transfer to the adsorbed oxygen to reduce to H_2O [26]. In addition, the participation of *f*-orbitals of Ce can induce unique electronic behavior to the catalyst that helps to form stable coordination structures with N-doped carbons. The Ce-based catalyst is known for its resistance to Fenton-type reactions, in which Cerium atoms deactivate the H_2O_2 that is formed due to a 2 + 2 electron reduction process. Especially, the Fe-N-C catalysts produce $OH^{\bullet}$ by the Fenton reaction [27]. The produced $OH^{\bullet}$ species are harmful to the catalyst and nafion membrane, and aggravates corrosion of the carbon, therefore drastically reducing the catalyst stability. Unlike the Fe-N_4-C catalyst, the Ce-N_4-C catalysts, due to their oxygen storage and easier release properties, help in effectively deactivating the $OH^{\bullet}$ [28].

Considering these advantages, in this work, we attempted to understand the effect of Ce atoms on the ORR in acidic electrolyte of 0.1 M $HClO_4$ aqueous solution. The Ce-N-C catalyst was synthesized by a traditional ZIF-based metal–organic framework and a pyrolysis approach. The synthesized catalysts were systematically characterized by both physiochemical and electrochemical methods. SEM images show the dodecahedron-shaped Ce-ZIFs, and the TEM images show the porous carbon with atomically dispersed Ce and N atoms, which are revealed by the elemental mapping. The XRD analysis shows no evidence of Ce in any of the nanoparticles formed, and thus we believe that the Ce atoms are well incorporated into the carbon matrix, in the form of atomic dispersions. The XPS analysis shows clearly the redox states of the Ce in the form of its Ce^{3+} and Ce^{4+} oxidation states. The ORR analysis indicates that the Ce/N-C-3 catalyst shows superior ORR activity in relation to the Pt/C catalyst, both in terms of kinetic activity and stability. When used as an ORR catalyst in dual-chamber microbial fuel cells (DCMFCs), the Ce/N-C-3 catalyst shows appreciable amounts of organic matter degradation, as evaluated by total organic carbon (TOC) analysis.

2. Results

The Ce-N-C catalyst is synthesized from a traditional metal–organic framework-derived ZIF, from Zn^{2+} and Ce^{3+} as metal ions and 2-methyl imidazole (2-MIM) as organic ligand, in a methanolic solution. The optimum content of Ce is optimized by varying the Ce^{3+} precursor amount introduced during the ZIF formation. The synthesized Ce-ZIF is then pyrolyzed in N_2 atmosphere at 950 °C to obtain the Ce-N-C catalysts (Scheme 1).

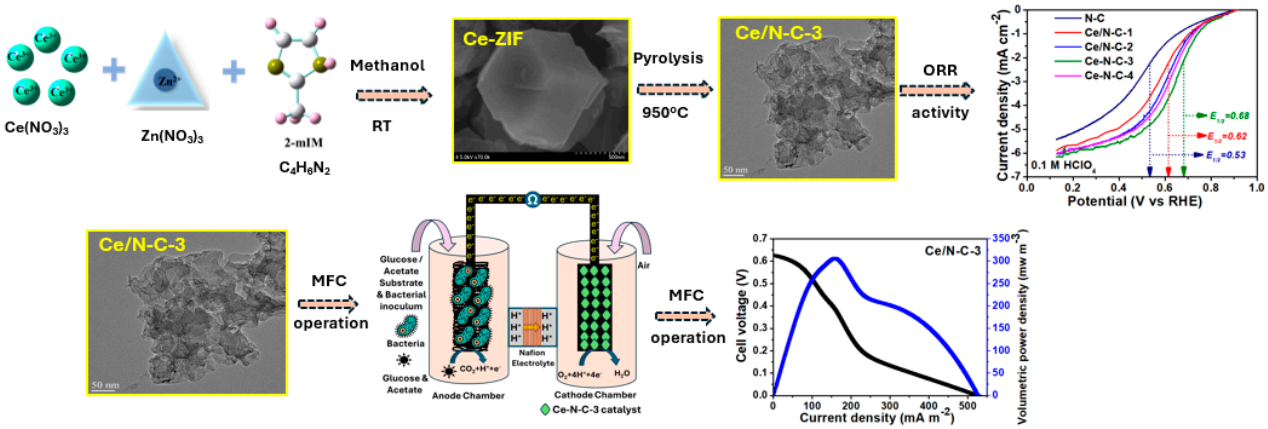

Scheme 1. Schematic representation of the Ce/ZIF and Ce/N-C- catalyst synthesis and their ORR and MFC performance analysis.

Figure 1a shows the XRD patterns for N/C and Ce/N-C-3 catalysts, which indicate typical diffraction patterns of carbon materials with a diffraction peak centered around ~25° and ~44°, corresponding to the C (0 0 2) and C (1 0 1) planes, respectively. No visible peaks of any metallic components of Ce, either in the form of metallic/oxide/hydroxide/nitrides have been observed, indicating that the catalysts are purely composed of N-doped carbon and atomic dispersion of Ce atoms incorporated in the N-doped carbon matrix. Figure 1b–d show the Ce-ZIF-8 nanoparticles, which show a typical cubical dodecahedron structure of agglomerated Ce-ZIF-8 nanoparticles with an almost uniform size, indicating that insertion Ce did not typically alter the native ZIF-8 morphological structure [29]. The elemental mapping from the SEM-EDS analysis clearly indicates a dense distribution of Ce, suggesting a sufficient amount of Ce in the catalysts (Figure S1). We have now added fresh images to the supporting information of the article. It can be seen that the Ce/N-C sample contains a sufficient amount of Ce atoms. The BET analysis of the Ce/N-C-3 catalyst (Figures S2 and S3) and found that it has a surface area of ~899 m^2 g^{-1} and BJH pore size distribution analysis reveals most of the pores in the catalyst are in the range of 3–5 nm, with an average pore diameter of 3.8 nm which is within mesoporous range. Therefore, it confirms that the Ce/N-C-3 catalyst has mesoporous range. Figure 2a–d show the TEM images of the Ce/N-C-3 catalyst. TEM images confirm the porous nature of the carbon derived from the pyrolysis of the Ce-ZIF MOFs. Furthermore, no visible agglomeration of Ce nanoparticles in any of the metallic/oxide/hydroxide/nitrides is apparent, which gives clear evidence that the metallic Ce is possibly atomically dispersed in the carbon matrix [30]. The HAADF images and corresponding elemental mapping of C, O, N, and Ce for the Ce/N-C-3 indicates that the catalyst contains the C and N and dispersed Ce atoms (Figure 2e–j). Furthermore, line mapping of the Ce/N-C-3 catalyst in a particular region reveals that the catalyst contains the N and Ce atoms, which exist together in the observed region. Figure 2k,l further reveals that there is a possibility of the formation of Ce-N_4-C structures similar to the M-N_4-C structure that is observed in the case of Fe and Co catalysts, which are believed to be the actual ORR active sites in the metal–N-doped carbons.

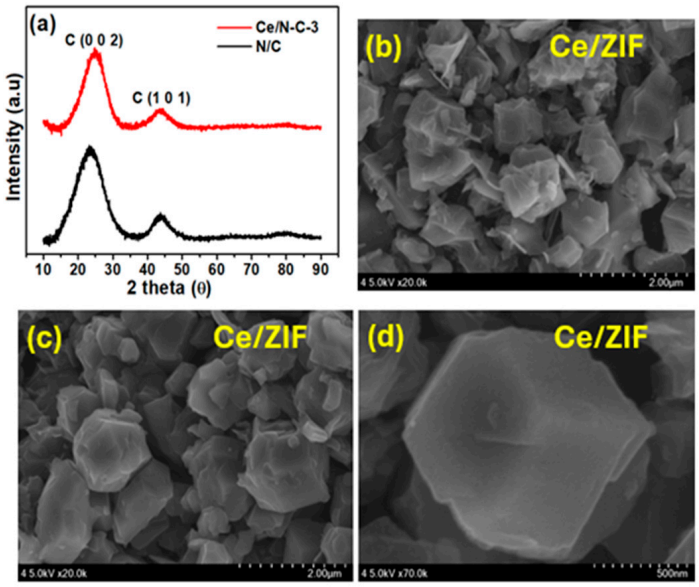

Figure 1. (**a**) X-ray diffraction images of the N/C and Ce/N-C-3 catalysts. (**b**–**d**) SEM images of the Ce/ZIF precursor.

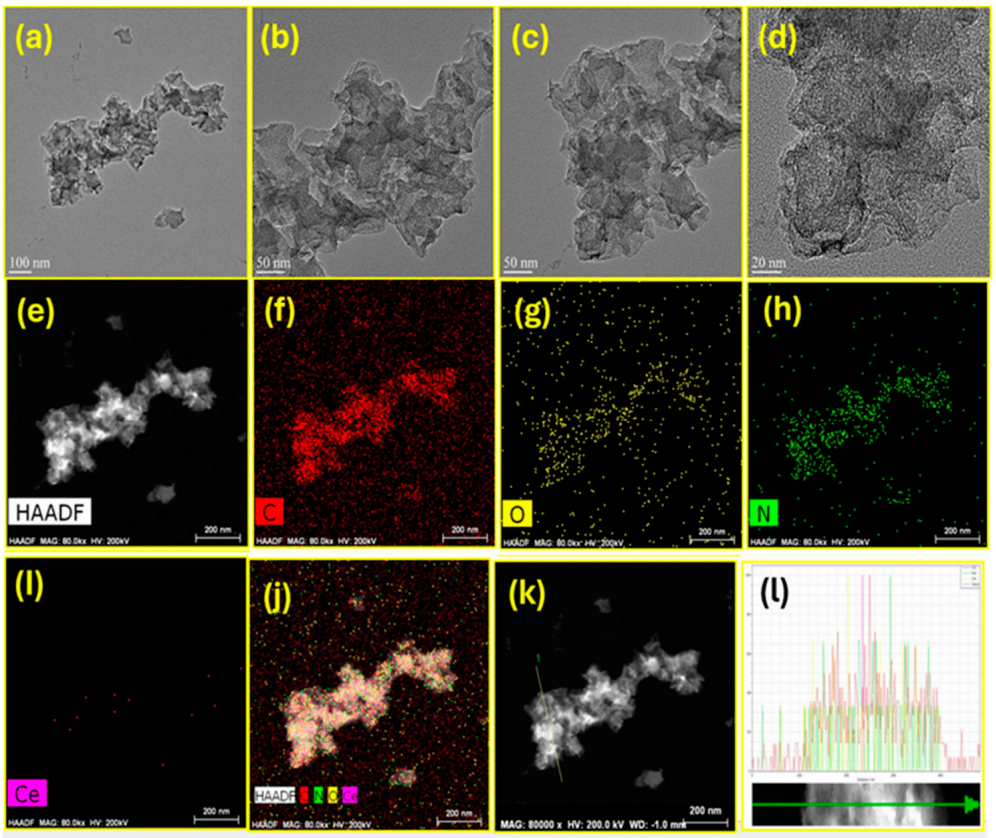

Figure 2. (**a**–**d**) TEM images of the Ce/N-C-3 catalysts. (**e**) HAADF image and corresponding elemental mapping of (**f**) carbon, (**g**) oxygen, (**h**) nitrogen, (**i**) cerium, (**j**) overall mapping of all the elements in the Ce/N-C-3 catalysts, and (**k**) line-mapping image and (**l**) corresponding line mapping of the elements in a particular region of the Ce/N-C-3 catalyst.

XPS analysis of the Ce/N-C-3 catalyst provides insights into the oxidation states of the elements such as C, N, and Ce. Figure 3a shows the XPS spectra for C1s in the Ce/N-C-3 catalyst, which can be deconvoluted into four major peaks at the binding energies of 284.84,

285.44, 286.44, and 288.64 eV, for C-C, C=O, O-C=O, and -C-N bonding states in the catalyst, respectively. The presence of C-C and C=C indicates that the catalyst contains both sp3 and sp2 carbon, respectively [31]. This indicates that the carbon contains both graphitized and defective carbon, arising from the presence of O and N in the catalysts. In addition, the appearance of C-N confirms the presence of N in the catalysts that is derived from the N atoms in 2-MIM, incorporated into the carbon matrix during pyrolysis. Figure 3b shows the XPS spectra for N1s in the Ce/N-C-3 catalyst, which can be deconvoluted into four major peaks at the binding energies 397.58, 398.18, 398.88, and 400.68 eV for pyridinic-N, possible pyridinic-N-Ce, pyrrolic-N, and graphitic-N electronic states in the Ce/N-C-3 catalyst, respectively [32]. Each of these electronic states of N significantly contributes to the intrinsic ORR activity, which comes exclusively from the N doping. Generally, the pyridinic-N can be found at the carbon plane edges, which also contributes its lone pair of electrons to the carbon, thus enhancing the electronic conductivity. In addition, the pyridinic-N also helps in the adsorption of O_2 and donation of its unpaired electrons to the O_2, thus weakening the O=O bond and subsequently reducing it into H_2O [33]. Generally, the pyrrolic-N is situated in the defect sites of the carbon and is incorporated into the five-member ring of the carbon matrix, contributing its unshared electron pair to the carbon π electron density, thereby increasing the electronic conductivity of the carbon support and consequently enhancing the activity of the ORR [34]. Graphitic-N, on the other hand, is situated in the basal plane of the carbon matrix, which alters the electronic charge density/spin density around the carbon atoms, and hence acts as a potential ORR active site [35]. Interestingly, the appearance of the peak at the binding energy of 398.88 eV is possibly due to the formation of pyridinic-N-Ce bonding structures, similar to the Fe-N_4-C [36]. It is well known that pyridinic-N, compared to pyrrolic-N and graphitic-N, has a higher chemical reactivity for trapping metal atoms like Ca, Al, Mg, Fe, Co, Mn, La, Ce, Y, etc., to defect sites due to the distinct local charge distribution in the presence of lone pair electrons. Besides stabilizing metal atoms, pyridinic-N-Ce bonding structures boost carbon-based catalyst ORR activity. The metal atom anchored on three or four pyridinic-N doped graphene vacancy sites, MN_3C and MN_4C, are studied mostly for their low formation energies and superior electronic properties. According to studies, MN_4C is more stable than MN_3C due to more M-N bond formations, but highly reactive for ORR [37–40]. The presence of pyridinic-N on the edges has been extensively recorded as potential sites for the coordination of metallic ions, resulting in the formation of Ce-N_4-C structures [41]. This facilitates optimal adsorption and efficient reduction of O_2 due to the synergistic effect of both N- and Ce. From the XPS analysis, its clearly visible that Ce is bonding with N, therefore it is reasonable to assume that there are high possibilities for the formation of the Ce-N_4-C structure; it is very common and usually interpreted from the XPS analysis, and the primary evidence for Ce-N_4-C structures in the catalysts; this is consistent with the literature [37–41]. Therefore, the formation of potential Ce-N_4-C could be possible active sites in the Ce/N-C-3 catalyst; however, further detailed studies with sophisticated analytical instruments such as X-ray absorption near-edge structure (XANES) and Fourier transform-extended X-ray absorption fine structure (FT-EXAFS) spectra are required to confirm the Ce-N_4-C structures. The N atoms in the carbon matrix contribute electrons to the Ce atoms, resulting in an increased electron density around the Ce atom. This electron density can then be transferred to the adsorbed O_2, causing a weakening of the O=O bond and subsequent reduction to water, H_2O. In particular, bonding between carbon and cerium C-N_4-Ce is observed at the edges of the pores when four nitrogen atoms from four different pyridinic-N groups come together to form Ce-N_4-C structures. These Ce-N_4-C structures are believed to be the active sites for the ORR in several single-atom catalysts such as Fe-N_4-C and Co-N_4-C, including Ce-N_4-C [42,43]. Figure 3c shows the XPS spectra for Ce 3d spectra in the Ce/N-C-3 catalyst, which can be deconvoluted into six peaks resulting from the triplet peaks, one each for the Ce $3d_{3/2}$ and Ce $3d_{5/2}$ electronic states. The Ce $3d_{3/2}$ peak exhibits additional splitting into three distinct peaks at 906.38, 904.18, and 901.18 eV, which correspond to the presence of Ce^{4+}, Ce^{3+}, and Ce^{3+} ions,

respectively. Similarly, the Ce $3d_{5/2}$ peak can be separated into distinct peaks at 886.78, 884.68, and 882.28 eV, which are associated with Ce^{4+}, Ce^{3+}, and Ce^{4+} ions, respectively. The XPS spectra verifies the simultaneous presence of Ce^{4+} and Ce^{3+}, facilitating efficient charge transfer during ORR by means of the continuous interconversion between Ce^{4+} and Ce^{3+}. In addition, the interconversion between Ce^{4+} and Ce^{3+} helps to deactivate the $OH^{\bullet}$ during the ORR [44].

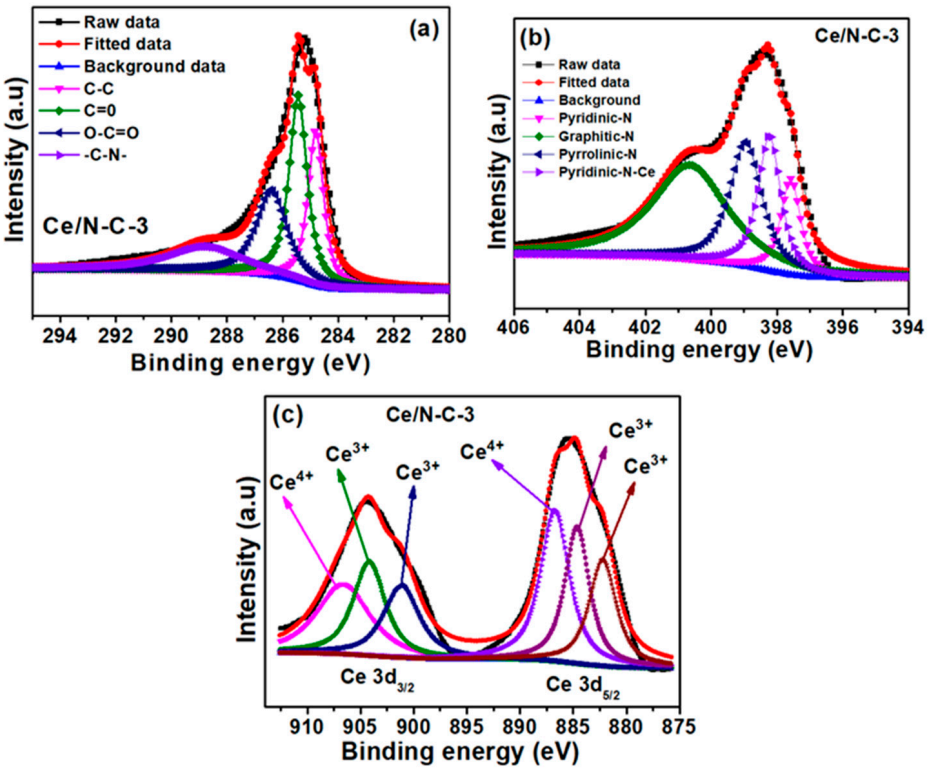

Figure 3. Deconvoluted spectra of (**a**) C1s, (**b**) N 1s, and (**c**) Ce 3d elements in the CE/N-C-3 catalysts.

After analyzing the Ce/N-C catalysts for their physicochemical characterization, the catalysts are then assessed for ORR in 0.1 M $HClO_4$ electrolyte. The optimum content of the Ce in the N-doped carbon matrix has been evaluated by varying the Ce precursor concentration during the ZIF synthesis. The assumption is that the Ce loading in the catalysts would linearly increase with the amount of Ce precursor used. This assumption is based on the expectation that a higher concentration of Ce precursor would result in a greater incorporation of Ce^{3+} ions into the ZIFs, which would then be retained in the carbon matrix after pyrolysis. This linear relationship is also reflected in the observed increase in half-wave potentials with higher Ce concentrations, as shown in Figure 4. The optimum content of Ce is then assessed through the ORR activity. Figure 4a shows the LSV curves of the Ce/N-C catalyst in O_2 saturated 0.1 M $HClO_4$ electrolyte at 1600 rpm. All the catalysts show a typical ORR characteristic with kinetic, mixed kinetic diffusion-controlled, and limiting currents. We derived the half-wave potential ($E_{1/2}$) values for all the catalysts to assess the catalysts' ORR activity. Interestingly, the N-C catalyst shows an $E_{1/2}$ of 0.53 V, therefore confirming the intrinsic ORR activity of the carbon matrix due to N dopants. It is well known that N dopants alters the change and spin density of the nearby carbons atoms and thus helps to absorb the O_2 [45]. N-doping also increases the electronic conductivity of the carbon, therefore collectively helping in the reduction of O_2 to H_2O. Further, when Ce atoms are introduced into the carbon N-doped carbon matrix, it is observed that the ORR activity increased, possibly due to the formation of Ce-N_4-C active sites. The obtained $E_{1/2}$ potentials are 0.62, 0.67, 0.68, and 0.65 V for the Ce/N-C-1, 2, 3, and 4 catalysts, corresponding to 24/48/72/96 mg of the $Ce(NO_3)_2$ precursor, respectively.

It can be clearly seen that the $E_{1/2}$ steadily increases with the increase in Ce content, due to increased Ce atom concentration in the catalyst. With the incorporation of Ce atoms, a total gain of 150 mV in the $E_{1/2}$ potentials (Ce/N-C-3) is observed, in comparison to the N-C catalyst. These results clearly suggest that the incorporation of Ce has a definite role in enhancing the O_2 adsorption and reducing the O_2 to H_2O, due to its unique f-orbital Ce that can induce unique electronic behavior to the catalyst, which then helps to form stable coordination structures with N-doped carbons (Ce-N_4-C active sites) and its unique redox switching ability (Ce^{3+}/Ce^{4+}) [46].

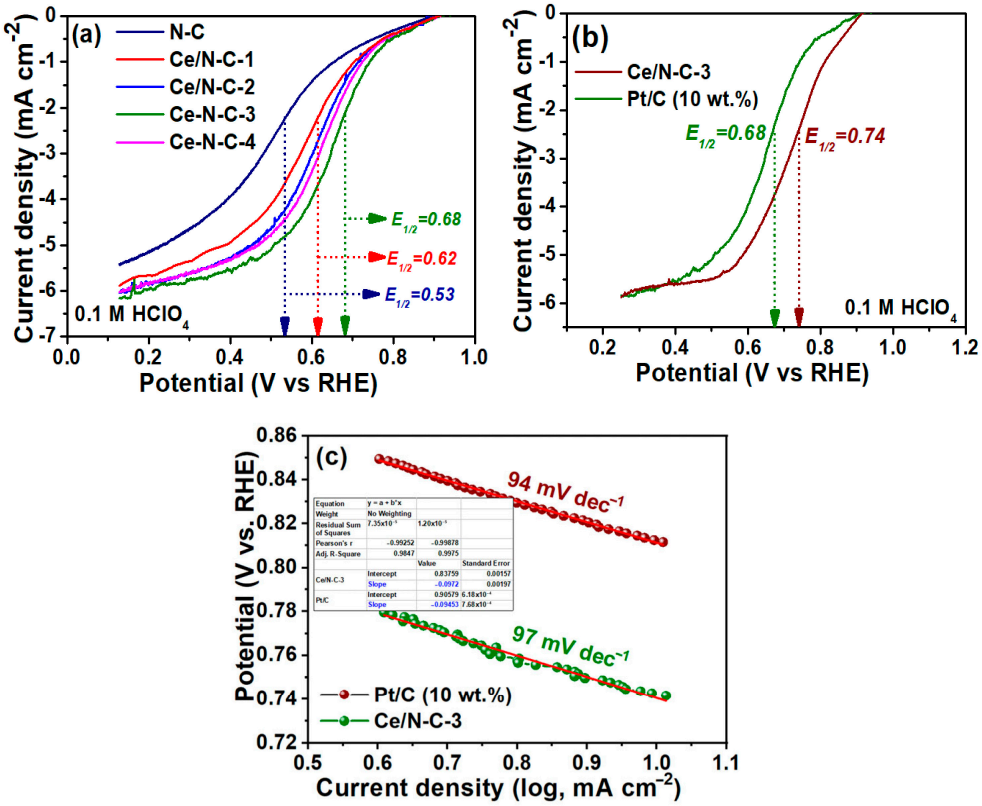

Figure 4. (**a**) LSV curves of the Ce/N-C-1,2,3 and four catalysts along with N-C catalyst. (**b**) LSV comparison of Ce/N-C-3 and Pt/C (10 wt.%) catalyst. (**c**) Tafel slopes of the Ce/N-C-3 and Pt/C (10 wt.%) catalyst. Electrolyte: O_2-saturated 0.1 M $HClO_4$, scan rate 10 mV sec^{-1}, 1600 rpm.

The optimized Ce/N-C-3 is then compared with the state-of-the-art ORR catalyst, Pt/C (10 wt.%) as shown in Figure 4b. The Pt/C (10 wt.%) catalyst shows a half-wave potential of 0.74 V. However, the ORR activity of Ce/N-C-3 catalyst is still inferior to Pt/C (10 wt.%) by 60 mV. The Ce/N-C-3 catalyst being non-precious, however, indicates that the ORR activity obtained is still considered as appreciable, with further opportunities to increase the ORR activity by incorporating additional metal active sites composed of other rare earth metals/transition metals. The dual metal atom catalysts have recently been shown to enhance the ORR kinetics more than the single metal catalysts, due to synergistic effect by different metal active sites and unique electronic states offered by dual metals. Therefore, we believe the ORR activity of the Ce/N-C-3 catalyst can be further enhanced by incorporation of a second metal. Figure 4c shows the Tafel analysis of the Pt/C (10 wt.%) and Ce/N-C-3 catalysts. The obtained Tafel values were 94 and 97 mV dec^{-1} for Pt/C (10 wt.%) and Ce/N-C-3 catalyst, suggesting that ORR proceeds by a similar mechanism on Ce/N-C-3 catalyst, just like Pt/C, in which adsorption of O_2 along with the first electron/proton transfer is a rate-determining step. The Tafel values indicate that the ORR proceeds through similar ORR kinetics, with the first electron transfer being the rate-determining step for both catalysts; however, the overpotential for Ce/N-C-3 catalysts

is observed to be still higher than the Pt/C, possibly due to lower ORR activity of the Ce/N-C-3 catalyst when compared to the Pt/C (10 wt.%) catalyst, as seen in Figure 4b.

The optimized catalysts are further evaluated for the ORR mechanistic pathway by recording LSVs at different rpms and deriving their K-L plots for calculating the number of electrons transferred per O_2 molecule. Figure 5a–c show the LSV recorded at different rotations per minute. It is seen that for all three catalysts, limiting current steadily increases with an increase in the rotations per minute, whereas there is hardly any difference in the kinetic regions of the LSV curves. This clearly suggests that the ORR is a diffusion-controlled reaction, which requires gaseous O_2 reactant to diffuse from the bulk solution to the catalyst surface to become adsorbed, in order to be reduced on the electrocatalyst surface. The K-L plots were derived from the LSVs recorded from different rpms by plotting the inverse of the current density and the inverse square root of the rotation speed, as shown in Figure 5d–f. The derived K-L plots are found to be almost linear at different potentials for all the Ce/N-C-3 and Pt/C catalysts, whereas slightly scattered plots for the N-C catalyst. This indicates that all the catalysts follow a similar reaction mechanism which remains almost constant across the potential ranges. The linear K-L plots also indicate that the overall ORR is influenced by both kinetic and diffusion-controlled processes. The average number of electrons transferred per O_2 molecule is found to be 3.64, 3.91, and 3.98 for the N-C, Ce/N-C-3 and Pt/C (10 wt.%) catalysts. This indicates that the ORR proceeds through a dominant direct 4-electron O_2 reduction reaction, which results in the formation of H_2O. The direct 4-electron reduction is a desired reaction pathway for any catalyst to be used in fuel cells. Other reaction pathways result in a 2 + 2-electron reduction, which forms H_2O_2 as an undesired product of O_2 reduction. Concerning this observation, it is noted that the Ce-N-C catalyst comes with the additional advantage of deactivating any negligible amount of H_2O_2 due to its redox ability. This property of scavenging of the $H_2O_2/OH^{\bullet}$ by Ce/N-C is especially helpful to maintain the stability of the catalysts and electrolyte membrane [47,48].

Figure 6 shows the stability results, assessed by potential cycling of the catalysts in acidic electrolytes in the potential range of 0.0 to 1.23 V vs. RHE. Figure 6a shows the cyclic voltammogram of the Pt/C catalyst, presenting a typical voltammogram of the hydrogen adsorption/desorption region and capacitive regions. The potential cycling of the catalysts were carried out for 5000 cycles. It is observed that the integrated area under the hydrogen adsorption/desorption region linearly decreases with increase in the potential cycling, representing the decreased electrochemically available surface area of the Pt nanoparticles, in the Pt/C catalyst. It is well known that poor stability of the Pt/C catalyst in acidic electrolyte is due to Pt nanoparticle dissolution, re-deposition, and agglomeration of the P nanoparticles that leads to decreased electrochemically active surface area (ECSA) [49]. The degradation is further quantified for Pt/C catalyst ECSA measurements before and after cycling. Initially, ECSA was 60.9 m^2/g Pt. After cycling, ECSA dropped to 50.2 m^2/g Pt and then to 41.5 m^2/g Pt. This significant ECSA reduction is due to active Pt surface area loss and the degradation mechanisms such as coalescence, Pt nanoparticle dissolution, re-deposition, and agglomeration. The decreased ECSA indicates decreased catalytic activity and shows the effect of potential cycling that affects the Pt/C catalyst performance. The corresponding LSV curves, recorded after 2500 and 5000 cycles, show clear evidence of poor stability of the Pt/C catalyst, due to the reduction in the ORR activity in terms of the loss in the half-wave potential. The Pt/C catalyst lost 60 and 110 mV from its initial ORR activity, after 2500 and 5000 cycles, respectively (Figure 6b). In addition, one can see that after 5000 potential cycles, the Pt/C LSV curves show the typical two plateaus after cycling, representing a shift in the reaction pathway from a direct 4-electron O_2 reduction to an indirect 2 + 2-electron and 4-electron mixed O_2 reduction pathway. We believe that poor stability of the Pt/C catalysts leads to the LSV curves having two plateaus after cycling. During the stability test, by losing Pt nanoparticles during cycling, more carbon surface is exposed. The carbon matrix is known to perform the ORR through a less efficient 2 + 2-electron reduction pathway than Pt nanoparticles' direct 4-electron process.

Increased H_2O_2 production may result from this change in reaction mechanism. Thus, the two LSV plateaus may represent the ORR activities of the remaining Pt nanoparticles and the exposed carbon surface. The initial plateau indicates ORR on remaining Pt sites, while the second plateau is caused by ORR on the carbon surface, producing H_2O_2 [50]. In contrast, under similar experimental conditions, the Ce/N-C-3 catalyst shows improved catalyst stability, as shown in Figure 6c,d. The Ce/N-C-3 catalyst shows excellent ORR characteristics even after 5000 potential cycles. The Ce/N-C-3 catalyst shows the loss of 30 and 70 mV from its initial ORR activity after 2500 and 5000 cycles, respectively. Overall, after 5000 potential cycles, the Ce/N-C-3 catalyst lost 70 mV, whereas Pt/C lost 110 mV, in the half-wave potential values. These results indicate that the Ce/N-C-3 catalyst shows better stability than the Pt/C catalyst. In contrast to Pt/C catalyst morphology, where Pt nanoparticles are on the carbon support, mostly by weak metal–support interaction, in Ce/N-C-3 catalyst the Ce atoms are tightly bonded to the N-atoms of the carbon support (Ce-N_4-C structures). Therefore, the mechanism associated with the metal nanoparticle coalescence, dissolution, detachment, and re-deposition are expected to occur very slowly. Therefore, Ce atom leaching or detachment is prevented; thus, the Ce/N-C-3 catalyst performs better in the stability test when compared to Pt/C catalysts. However, the other mechanisms of degradation, such as carbon corrosion, still occur in Ce/N-C-3, and that might be the reason that the Ce/N-C-3 catalyst CVs are more resistive after cycling and also the reason for reduction in the half-wave potentials.

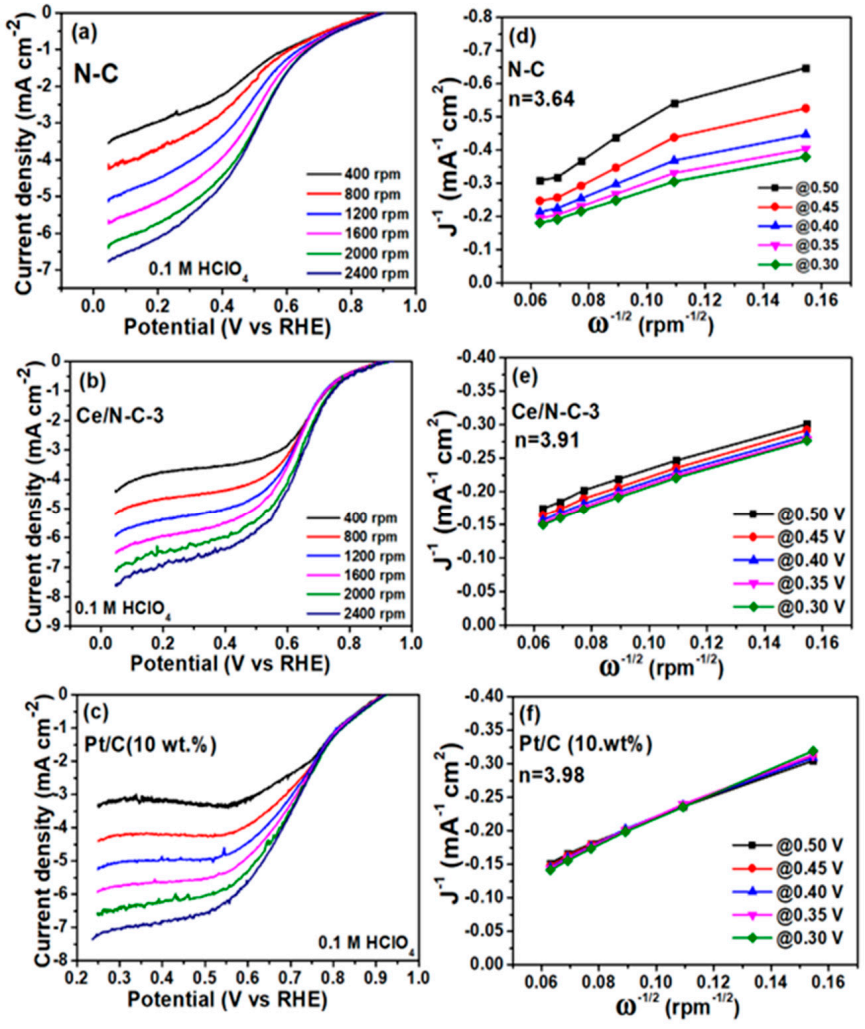

Figure 5. LSV curves recorded at different rpms of the catalysts and their corresponding K-L plots for the N-C (**a**,**d**), Ce/N-C-3 (**b**,**e**), and Pt/C (**c**,**f**) catalysts.

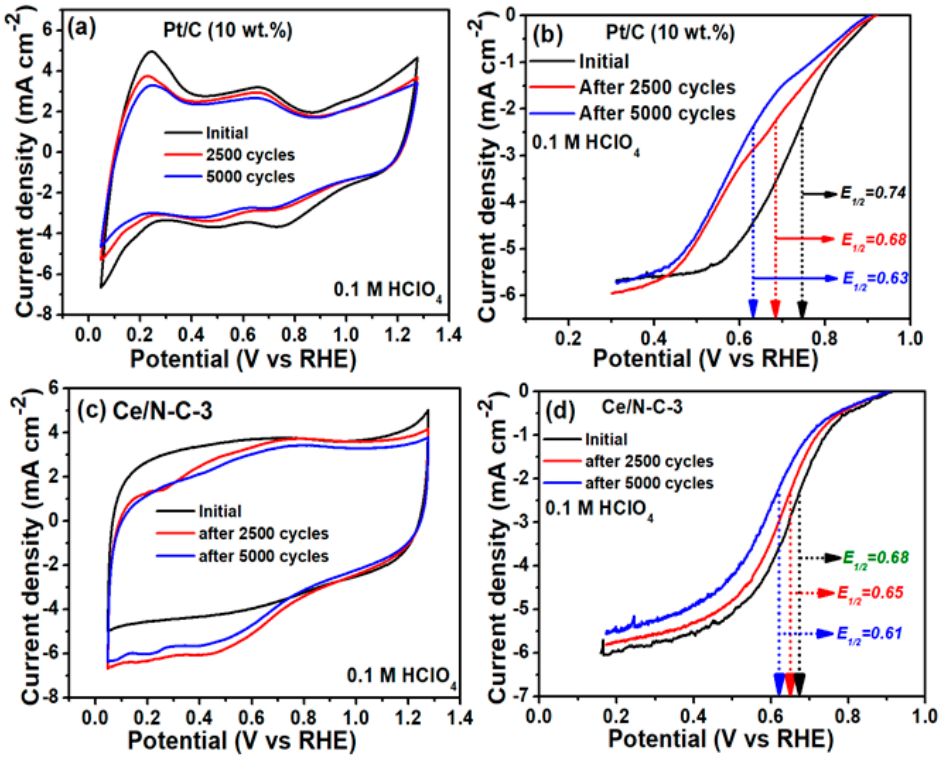

Figure 6. Stability analysis of the Pt/C and Ce/N-C-3 catalysts. Cyclic voltammograms of the (**a**) Pt/C and (**c**) Ce/N-C-3 catalysts. (**b**) Linear sweep voltammetry curves of the (**b**) Pt/C and (**d**) Ce/N-C-3 catalysts. The stability conditions are 0.1 M $HClO_4$ aqueous solution as the electrolyte. Scan rate for CV cycling test 50 mV sec^{-1}; LSV: scan rate 10 mV sec^{-1}; 1600 rpm in O_2-saturated 0.1 M $HClO_4$. All the tests were conducted at 25 °C.

After a detailed electrochemical analysis of the catalysts for ORR activity and stability, we finally evaluated the microbial fuel cell performance for the Ce/N-C-3 catalyst. A catalyst loading of about 2.5 mg cm^{-2} was achieved by brush coating on commercial gas diffusion layers with a catalyst ink made of the Ce/N-C-3 catalyst. The performance of the MFC was evaluated in a brush anode and a previously activated DCMFC cell that had been inoculated with bacteria derived from local drainage sewage water sludge and a carbon source mixture of sodium acetate and glucose. Once the cathode catalyst was added to the phosphate buffer solution (PBS), we filled the cathode compartment, which was continuously purged with atmospheric air (Figure 7a). OCV was then generated and gradually increased over time and stabilized after a while. The i–v curves were only recorded after the voltage had stabilized. Another experiment was conducted to assess the performance of the MFC using a gas diffusion layer coated with Pt/C. This was carried out compare the performance of the Ce/N-C-3 catalyst with the state-of-the-art Pt/C catalyst. Figure 7b shows the OCV values of the Ce/N-C-3 and the Pt/C catalyst, which indicate that initial OCV values were around ~0.4 V and ~0.52 V for the Pt/C and Ce/N-C-3 catalysts, which were steadily increased to final and stabilized OCV values of ~0.69 and ~0.63 V for the Pt/C and Ce/N-C-3 catalysts, respectively. Figure 7c shows the i–v curve for the Pt/C catalyst, which delivered a volumetric power density of 638 mW m^{-3}, with an acetate+glucose mixture as the carbon source and atmospheric air saturated in PBS buffer as the oxidant. Under similar operating conditions, the Ce/N-C-3 catalyst delivered a volumetric power density of 306 mW m^{-3}, approximately half the power density of the Pt/C catalyst (Figure 7d).

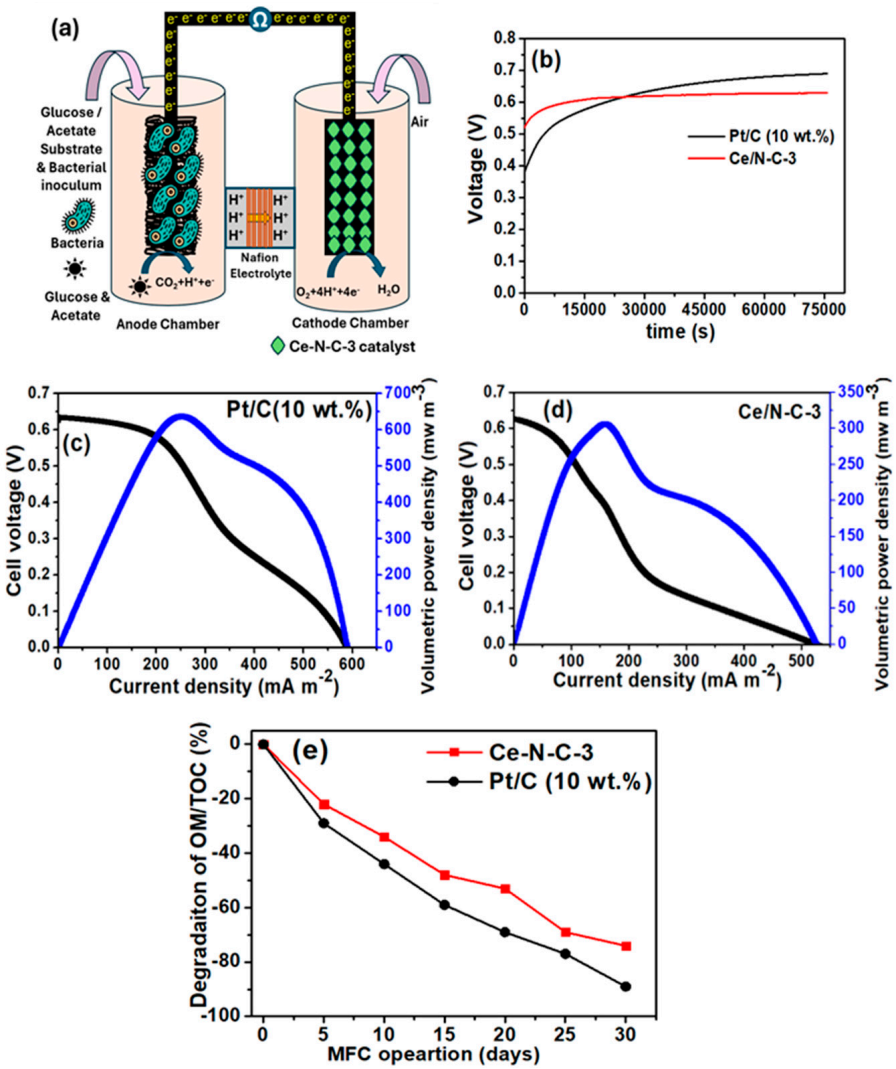

Figure 7. (**a**) Schematic operation of the dual-chamber microbial fuel cells set up and used in this study: (**b**) OCV values of Pt/C and Ce/N-C-3 catalysts; (**c**,**d**) i–v curves for Pt/C and Ce/N-C-3 catalysts; (**e**) TOC analysis of the anolyte of the microbial fuel cells with Pt/C and Ce/N-C-3 as the cathode catalysts.

The low MFC performance could be attributed to various mixed and complex processes and phenomenon both from anodes and cathodes. Concerning the anodes, MFC performance can be affected by the type and density of the bacterial electroactive species that are capable of efficiently transferring electrons from the bacterial cell to the anodes. In this case, the inoculum of the bacterial culture is very important. Here, we used drainage water collected from the local underwater pipeline as the inoculum (to mimic the actual case of wastewater characteristics), although it might not contain an optimal concentration of the electroactive bacteria. In addition, the bacterial species in the local drainage wastewater might have a low metabolic rate or might not be well adapted to the substrate (in this case glucose and acetate), as each bacterial species is substrate specific. There could also be a high chance of bacterial competition, which would result in the overgrowth of some species of bacteria compared to others. In addition to these factors, the type of anode and its electrical conductivity, the geometrical area of the anode, the reactor design, and the membrane fouling/clogging also affect the MFC performance. Concerning the cathode side, the conductivity of the substrate, the ORR activity of the cathode catalysts, the loading of the cathode catalysts, and the geometrical area of the cathode electrode, along with the type of oxidant (O_2 vs. air) and their flow rates could affect the overall

MFC performance. Though the performance of the MFC with the Ce/N-C-3 catalyst is just half of the performance of the Pt/C catalyst, we believe that further enhancement in the performance of the Ce/N-C-3 catalyst could be realized with either optimizing the MFC performance with further increase in the catalyst loading, optimizing the ionomer ratio, or by exploring the alternative substance to the traditional carbon paper with carbon brush, carbon cloth, and carbon felt. Enhancing the performance can also be achieved by introducing a secondary rare earth metal or transition metal along with the Ce, to obtain an advantage in the synergistic effect in improving the overall ORR performance. In addition to the MFC performance, we also evaluated the ability of the MFC in degrading organic matter in wastewater streams by analyzing the total organic carbon (TOC) of the anolyte in the anode compartment. For this, an ample anolyte was collected for an interval of 3 days, with the MFC being operated continuously with placement of a 100 Ω resistor. The collected anolyte was immediately analyzed by the TOC instrument; the results are shown in Figure 7d. It is seen that TOC values gradually decreased with time, both for the Ce/N-C-3 and Pt/C (10 wt.%) catalysts. After 30 days continuous operation of the MFCs, the MFC with the Pt/C catalyst could degrade ~89% of the organic matter, whereas the MFC operated with the Ce/N-C-3 catalyst could degrade ~74% of the organic matter. This proves that the study's MFC with the Ce/N-C-3 catalyst developed in this study can efficiently break down organic materials while simultaneously producing an ample power density.

3. Materials and Methods

3.1. Synthesis of ZIF-8 Nanoparticles

The ZIF-8 nanoparticles were synthesized by the traditional methanol-solution-mediated synthesis approach; 5.3 g of $Zn(NO_3)_2$ and 6.4 g of 2-methyl imidazole (2-MIM) were dissolved in 20 mL of methanol solvent in separate beakers. The 2-MIM solution was added dropwise from the burette to the solution of $Zn(NO_3)_2$ under continuous magnetic stirring. The solution was then allowed to be magnetically stirred for about 6 h and a white precipitate formed, which was then collected by centrifugation and after repeated washing with methanol. The precipitate was then dried in a hot-air oven at 75 °C for about 10 h. The dried precipitate was then ground into a fine powder using a mortar and pestle, and then processed further for pyrolysis.

3.2. Synthesis of Ce-Incorporated Ce-ZIF-8 Nanoparticles

In this procedure, 5.3 g of $Zn(NO_3)_2$, 24/48/72/96 mg of $Ce(NO_3)_2$, and 6.4 g of 2-methyl imidazole (2-MIM) were dissolved in 20 ml of methanol solvent in separate beakers. The 2-MIM solution was added dropwise from the burette to the solution of $Zn(NO_3)_2$ and $Ce(NO_3)_2$ under continuous magnetic stirring. The solution was then allowed to be magnetically stirred for about 6 h and a white precipitate formed, which was then collected by centrifugation and after repeated washing with methanol. The precipitate was then dried in a hot-air oven at 75 °C for about 10 h. The dried precipitate was then ground into a fine powder using a mortar and pestle, and then processed further for pyrolysis.

3.3. Synthesis of the N-Doped Carbon and Ce-N-C Catalysts

The ZIF-8 and Ce-ZIF-8 powders were transferred to a graphite crucible and placed inside a tubular furnace. The furnace temperature was raised to 950 °C with a ramping of 5 °C/min increase in the temperature. Once the final temperature of 950 °C was achieved, it was maintained for about 1 h in the presence of continuous flow of N_2 inert gas. After pyrolysis, the black powdered catalyst was collected and then ground into fine powder and designated as ZIF-8 → N/C and Ce-ZIF-8 → Ce/N-C catalysts. In the Ce/N-C catalysts, the catalysts were further designed as Ce/N-C-1, 2, 3, and 4, corresponding to Ce loading of 24/48/72/96 mg of $Ce(NO_3)_2$.

3.4. Physicochemical and Electrochemical Characterization of the N/C and Ce/N-C Catalysts

The N/C and Ce/N-C catalysts were characterized by XRD studies for obtaining the defects and crystallinity of the catalysts, morphological analysis by SEM and TEM measurements, and oxidation states by XPS studies. The electrocatalytic ORR activity was assessed through a traditional three-electrode system using a glassy carbon electrode, a graphite rod, and a saturated calomel electrode as the working, counter, and reference electrodes respectively, in 0.1 M $HClO_4$ by using cyclic voltammetry, liner sweep voltammetry, and rotating disk electrode measurements. Justification for using a graphite rod as the counter electrode is given in the Supplementary Materials included with this article, Section S5. The organic matter degradation studies were then assessed for the final optimized catalysts in dual-chamber microbial fuel cells (DCMFCs) with the anode as a carbon brush and cathode made of carbon paper with the Ce-N-C and Pt/C catalysts. The organic matter degradation was then monitored by collecting an ample of anolyte made of a glucose+acetate mixture and analyzed by using the total organic carbon (TOC) technique (Scheme 1). The detailed experimental procedures for the physicochemical and electrochemical characterization of the N/C and Ce/N-C catalysts microbial fuel cell operation, instrumentation used for RDE/MFC studies, justification for using graphite rod as counter electrode, biofilm monitoring via OCV measurement over time are, given in the Supplementary Materials (S1–S6).

4. Conclusions

The Ce-incorporated dodecahedron-shaped ZIF particles were synthesized by a traditional methanolic solvent-mediated metal–organic framework strategy. The pyrolysis of the Ce-ZIF yields the atomically dispersed Ce atoms on the N-doped carbon support matrix. X-ray diffraction and transmission electron microscopic studies revealed no evidence for Ce atomic clusters/oxides/nanoparticles of the Ce; therefore, we assumed the Ce atoms were atomically dispersed. The XPS analysis revealed the possible formation of Ce-N_4-C structures due to the observed bonding between pyridinic-N and Ce atoms. The ORR activity of the Ce/N-C-3 catalysts was optimized by systematically increasing the Ce content and performing RDE studies in 0.1 M $HClO_4$ electrolyte. The optimized Ce/N-C-3 catalyst exhibited a half-wave potential of 0.68 V vs. RHE, equal to the ORR activity of Pt (10 wt.%). In addition, the Ce/N-C-3 catalyst also delivered acceptable stability with a loss of 70 mV in its half-wave potential when compared to 110 mV loss for Pt/C (10 wt.%) catalyst, after 5000 potential cycles. When Ce/N-C-3 is used as the cathode catalyst in dual-chamber microbial fuel cells, it delivered a volumetric power density of ~300 mW m^{-3}, along with an organic matter degradation of 74% after continuous operation of DCMFCs for 30 days.

Supplementary Materials: The following supporting information can be downloaded at: https://www.mdpi.com/article/10.3390/catal14080506/s1, S1: Physical and electrochemical characterizations; S2: Electrochemical Characterizations characterization of the Ce/N-C and NC catalysts; S3. Microbial fuel cell operation; S4. Instrumentation used for RDE/MFC studies; S5. Justification for using Graphite rod as the counter electrode; S6. Biofilm monitoring via OCV measurement over time; Figure S1: SEM images of Ce/N-C catalyst and the EDS elemental mapping, along with the tabular column reporting the atomic %t collected for each element in the catalyst, including Ce; Figure S2: N_2 adsorption/desorption isotherms of the Ce/N-C-3 catalyst; Figure S3: BJH desorption summary and the pore size distribution analysis of the Ce/N-C-3 catalyst. The RDE experimental procedures, including the catalyst ink preparation, loading, electrodes used, equations to calculate the number of electrons, the dual-chamber microbial fuel cell set up and procedures, analysis, and sample collection for TOC are given in this section.

Author Contributions: Conceptualization, S.A.; methodology, S.A.; validation, H.W.; formal analysis, S.G.P. and T.-G.L.; investigation, H.W.; resources, S.G.P. and T.-G.L.; data curation, H.W.; writing—original draft preparation, S.A.; writing—review and editing, S.G.P. and T.-G.L.; supervision, project administration, and funding acquisition, S.G.P. All authors have read and agreed to the published version of the manuscript.

Funding: The research was supported by the National Research Foundation of Korea (NRF), funded by the Korean Government, Ministry of Science and ICT (MSIT) (No. 2021R1F1A1046648), Republic of Korea.

Data Availability Statement: Data are contained within the article and Supplementary Materials.

Conflicts of Interest: The authors declare no conflicts of interest.

References

1. Babuji, P.; Thirumalaisamy, S.; Duraisamy, K.; Periyasamy, G. Human Health Risks due to Exposure to Water Pollution: A Review. *Water* **2023**, *15*, 2532. [CrossRef]
2. Hernández-Chover, V.; Castellet-Viciano, L.; Fuentes, R.; Hernández-Sancho, F. Circular economy and efficiency to ensure the sustainability in the wastewater treatment plants. *J. Clean. Prod.* **2023**, *384*, 135563. [CrossRef]
3. Waqas, S.; Harun, N.Y.; Sambudi, N.S.; Bilad, M.R.; Abioye, K.J.; Ali, A.; Abdulrahman, A. A Review of Rotating Biological Contactors for Wastewater Treatment. *Water* **2023**, *15*, 1913. [CrossRef]
4. Khalidi-Idrissi, A.; Madinzi, A.; Anouzla, A.; Pala, A.; Mouhir, L.; Kadmi, Y.; Souabi, S. Recent advances in the biological treatment of wastewater rich in emerging pollutants produced by pharmaceutical industrial discharges. *Int. J. Environ. Sci. Technol.* **2023**, *20*, 11719–11740. [CrossRef] [PubMed]
5. Sathya, R.; Arasu, M.V.; Al-Dhabi, N.A.; Vijayaraghavan, P.; Ilavenil, S.; Rejiniemon, T. Towards sustainable wastewater treatment by biological methods—A challenges and advantages of recent technologies. *Urban Clim.* **2023**, *47*, 101378. [CrossRef]
6. Jiang, W.; Zhang, J.; Yang, Q.; Yang, P. The Effect of Electricity Generation on the Performance of Microbial Fuel Cells for Anammox. *Sustainability* **2024**, *16*, 2705. [CrossRef]
7. Kunwar, S.; Pandey, N.; Bhatnagar, P.; Chadha, G.; Rawat, N.; Joshi, N.C.; Tomar, M.S.; Eyvaz, M.; Gururani, P. A concise review on wastewater treatment through microbial fuel cell: Sustainable and holistic approach. *Environ. Sci. Pollut. Res.* **2024**, *31*, 6723–6737. [CrossRef] [PubMed]
8. Zhang, H.; Duan, L.; Li, S.; Gao, Q.; Li, M.; Xing, F.; Zhao, Y. Simultaneous Wastewater Treatment and Resources Recovery by Forward Osmosis Coupled with Microbial Fuel Cell: A Review. *Membranes* **2024**, *14*, 29. [CrossRef] [PubMed]
9. Sonawane, A.V.; Rikame, S.; Gaikwad, M.; Bhanvase, B.; Sonawane, S.S.; Mungray, A.K.; Gaikwad, R. A review of microbial fuel cell and its diversification in the development of green energy technology. *Chemosphere* **2024**, *350*, 141127. [CrossRef]
10. Liang, B.; Su, M.; Zhao, Z.; Liang, S.-X. Iron-involved zeolitic imidazolate framework-67 derived Co/Fe-NC as enhanced ORR catalyst in air–cathode microbial fuel cell. *J. Electroanal. Chem.* **2024**, *962*, 118260. [CrossRef]
11. Jalili, P.; Ala, A.; Nazari, P.; Jalili, B.; Ganji, D.D. A comprehensive review of microbial fuel cells considering materials, methods, structures, and microorganisms. *Heliyon* **2024**, *10*, e25439. [CrossRef]
12. Dey, N.; Samuel, G.V.; Raj, D.S.; Gajalakshmi, B. Nanomaterials as potential high performing electrode materials for microbial fuel cells. *Appl. Nanosci.* **2022**, *13*, 2625–2640. [CrossRef]
13. Daud, N.N.M.; Ibrahim, M.N.M.; Yaqoob, A.A.; Yaakop, A.S.; Hussin, M.H. Evaluating the electrode materials to improve electricity generation with the removal of multiple pollutants through microbial fuel cells. *Biomass-Convers. Biorefinery* **2024**, 1–22. [CrossRef]
14. Peera, S.G.; Maiyalagan, T.; Liu, C.; Ashmath, S.; Lee, T.G.; Jiang, Z.; Mao, S. A review on carbon and non-precious metal based cathode catalysts in microbial fuel cells. *Int. J. Hydrogen Energy* **2021**, *46*, 3056–3089. [CrossRef]
15. Xu, G.; Yang, L.; Li, J.; Liu, C.; Xing, W.; Zhu, J. Strategies for improving stability of Pt-based catalysts for oxygen reduction reaction. *Adv. Sens. Energy Mater.* **2023**, *2*, 100058. [CrossRef]
16. Wang, Y.; Wang, D.; Li, Y. A fundamental comprehension and recent progress in advanced Pt-based ORR nanocatalysts. *SmartMat* **2021**, *2*, 56–75. [CrossRef]
17. Li, J.; Chen, Z. Revitalizing microbial fuel cells: A comprehensive review on the transformative role of iron-based materials in electrode design and catalyst development. *Chem. Eng. J.* **2024**, *489*, 151323. [CrossRef]
18. Bates, J.S.; Johnson, M.R.; Khamespanah, F.; Root, T.W.; Stahl, S.S. Heterogeneous M-N-C Catalysts for Aerobic Oxidation Reactions: Lessons from Oxygen Reduction Electrocatalysts. *Chem. Rev.* **2022**, *123*, 6233–6256. [CrossRef]
19. He, Y.; Tan, Q.; Lu, L.; Sokolowski, J.; Wu, G. Metal-Nitrogen-Carbon Catalysts for Oxygen Reduction in PEM Fuel Cells: Self-Template Synthesis Approach to Enhancing Catalytic Activity and Stability. *Electrochem. Energy Rev.* **2019**, *2*, 231–251. [CrossRef]
20. Yan, W.; Chen, W.; Chen, Y. Recent Design Strategies for M-N-C Single-Atom Catalysts in Oxygen Reduction: An Entropy Increase Perspective. *Adv. Funct. Mater.* **2024**, *240*, 1027. [CrossRef]
21. Peng, R.; Zhao, Z.; Sun, H.; Yang, Y.; Song, T.; Yang, Y.; Shao, J.; Jin, H.; Sun, H.; Zhao, Z. The Active Sites and Corresponding Stability Challenges of the M-N-C Catalysts for Proton Exchange Membrane Fuel Cell. *Chin. J. Chem.* **2023**, *41*, 710–724. [CrossRef]
22. de Araújo, M.A.; Koverga, A.A.; Sakita, A.M.P.; Ometto, F.B.; da Trindade, L.G.; Ticianelli, E.A. M−N−C Materials for Electrochemical Reduction Reactions: Recent Strategies for Improving Electrocatalytic Activity and Stability. *ChemCatChem* **2023**, *15*, e202201594. [CrossRef]

23. Wang, X.; Tang, Y.; Lee, J.-M.; Fu, G. Recent advances in rare-earth-based materials for electrocatalysis. *Chem Catal.* **2022**, *2*, 967–1008. [CrossRef]
24. Li, C.; Wang, P.; He, M.; Yuan, X.; Fang, Z.; Li, Z. Rare earth-based nanomaterials in electrocatalysis. *Coord. Chem. Rev.* **2023**, *489*, 215204. [CrossRef]
25. Filho, W.L.; Kotter, R.; Özuyar, P.G.; Abubakar, I.R.; Eustachio, J.H.P.P.; Matandirotya, N.R. Understanding Rare Earth Elements as Critical Raw Materials. *Sustainability* **2023**, *15*, 1919. [CrossRef]
26. Milikić, J.; Stojanović, S.; Damjanović-Vasilić, L.; Vasilić, R.; Šljukić, B. Efficient bifunctional cerium-zeolite electrocatalysts for oxygen evolution and oxygen reduction reactions in alkaline media. *Synth. Met.* **2023**, *292*, 117231. [CrossRef]
27. Zhang, H.; Wang, Y.; Song, D.; Wang, L.; Zhang, Y.; Wang, Y. Cerium-Based Electrocatalysts for Oxygen Evolution/Reduction Reactions: Progress and Perspectives. *Nanomaterials* **2023**, *13*, 1921. [CrossRef]
28. Liu, J.; Li, G.; Xu, C.; Chen, H.; Jin, R.; Sun, L.; Shu, C.; Chen, H.; Guo, C.; Li, H.; et al. Designing Ce single-atom-sites coupled with CeO_2 nanoparticles for oxygen reduction enhancement. *Inorg. Chem. Front.* **2023**, *10*, 3091–3102. [CrossRef]
29. Peera, S.G.; Lee, T.G.; Sahu, A.K. Pt-rare earth metal alloy/metal oxide catalysts for oxygen reduction and alcohol oxidation reactions: An overview. *Sustain. Energy Fuels* **2019**, *3*, 1866–1891. [CrossRef]
30. Salunkhe, R.R.; Young, C.; Tang, J.; Takei, T.; Ide, Y.; Kobayashi, N.; Yamauchi, Y. A high-performance supercapacitor cell based on ZIF-8-derived nanoporous carbon using an organic electrolyte. *Chem. Commun.* **2016**, *52*, 4764–4767. [CrossRef]
31. Dwivedi, N.; Yeo, R.J.; Satyanarayana, N.; Kundu, S.; Tripathy, S.; Bhatia, C.S. Understanding the Role of Nitrogen in Plasma-Assisted Surface Modification of Magnetic Recording Media with and without Ultrathin Carbon Overcoats. *Sci. Rep.* **2015**, *5*, 7772. [CrossRef] [PubMed]
32. Shaik, G.P.; Kwon, H.-J.; Lee, T.G. Highly efficient Co@NCS nanosheet electrocatalyst for oxygen reduction reaction: An environment-friendly, low-cost and sustainable electrocatalyst. *Mater. Res. Bull.* **2020**, *128*, 110873. [CrossRef]
33. Ning, X.; Li, Y.; Ming, J.; Wang, Q.; Wang, H.; Cao, Y.; Peng, F.; Yang, Y.; Yu, H. Electronic synergism of pyridinic- and graphitic-nitrogen on N-doped carbons for the oxygen reduction reaction. *Chem. Sci.* **2018**, *10*, 1589–1596. [CrossRef] [PubMed]
34. Xia, C.; Feng, J.; Ma, C.; Xi, H.; Song, N.; Dong, H.; Yu, L.; Dong, L. Exploring the underlying oxygen reduction reaction electrocatalytic activities of pyridinic-N and pyrrolic-N doped graphene quantum dots. *Mol. Catal.* **2023**, *535*, 112880. [CrossRef]
35. Wang, D.; Hu, J.; Wei, J.; Liu, X.; Hou, H. Insights into Nitrogen-doped Carbon for Oxygen Reduction: The Role of Graphitic and Pyridinic Nitrogen Species. *Chemphyschem* **2023**, *24*, e202200734. [CrossRef] [PubMed]
36. Jiao, L.; Wan, G.; Zhang, R.; Zhou, H.; Yu, S.H.; Jiang, H.L. From Metal–Organic Frameworks to Single-Atom Fe Implanted N-doped Porous Carbons: Efficient Oxygen Reduction in Both Alkaline and Acidic Media. *Angew. Chem. Int. Ed.* **2018**, *57*, 8525–8529. [CrossRef] [PubMed]
37. Zou, L.; Chu, W.; Cen, W. The coordination of Al on pyridinic-N doped graphene as electrons reservoir for efficiently catalyzing CO oxidization. *Appl. Surf. Sci.* **2020**, *531*, 147310. [CrossRef]
38. Peng, H.; Xie, X.; Sun, K.; Zhang, M.; Zhao, R.; Ma, G.; Lei, Z. Urea-assisted synthesis of a Fe nanoparticle modified N-doped three-dimensional porous carbon framework for a highly efficient oxygen reduction reaction. *New J. Chem.* **2020**, *44*, 6932–6939. [CrossRef]
39. Peng, H.; Mo, Z.; Liao, S.; Liang, H.; Yang, L.; Luo, F.; Song, H.; Zhong, Y.; Zhang, B. High Performance Fe- and N- Doped Carbon Catalyst with Graphene Structure for Oxygen Reduction. *Sci. Rep.* **2013**, *3*, 1765. [CrossRef]
40. Kabir, S.; Artyushkova, K.; Serov, A.; Kiefer, B.; Atanassov, P. Binding energy shifts for nitrogen-containing graphene-based electrocatalysts–experiments and DFT calculations. *Surf. Interface Anal.* **2016**, *48*, 293–300. [CrossRef]
41. Wang, X.-R.; Liu, J.-Y.; Liu, Z.-W.; Wang, W.-C.; Luo, J.; Han, X.P.; Du, X.-W.; Qiao, S.-Z.; Yang, J. Identifying the Key Role of Pyridinic-N-Co Bonding in Synergistic Electrocatalysis for Reversible ORR/OER. *Adv. Mater.* **2018**, *30*, e1800005. [CrossRef] [PubMed]
42. Lian, Y.; Xu, J.; Zhou, W.; Lin, Y.; Bai, J. Research Progress on Atomically Dispersed Fe-N-C Catalysts for the Oxygen Reduction Reaction. *Molecules* **2024**, *29*, 771. [CrossRef] [PubMed]
43. Hu, J.; Liu, W.; Xin, C.; Guo, J.; Cheng, X.; Wei, J.; Hao, C.; Zhang, G.; Shi, Y. Carbon-based single atom catalysts for tailoring the ORR pathway: A concise review. *J. Mater. Chem. A* **2021**, *9*, 24803–24829. [CrossRef]
44. Zhu, X.; Xie, S.; Fu, X.; Zhu, S.; Min, Y.; Xu, Q.; Li, Q. High-dispersion Co/N/C ultra-thin carbon nanosheets modified with trace Ce as efficient oxygen reduction reaction catalysts. *New J. Chem.* **2023**, *47*, 9153–9163. [CrossRef]
45. Ma, R.; Lin, G.; Zhou, Y.; Liu, Q.; Zhang, T.; Shan, G.; Yang, M.; Wang, J. A review of oxygen reduction mechanisms for metal-free carbon-based electrocatalysts. *npj Comput. Mater.* **2019**, *5*, 78. [CrossRef]
46. Tu, F.-D.; Wu, Z.-Y.; Guo, P.; Shen, L.-X.; Zhang, Z.-Y.; Dai, Y.-K.; Ma, M.; Liu, J.; Xu, B.; Zhang, Y.-L.; et al. Fe-N-C catalysts decorated with oxygen vacancies-rich CeOx to increase oxygen reduction performance for Zn-air batteries. *J. Colloid Interface Sci.* **2023**, *637*, 10–19. [CrossRef] [PubMed]
47. Siracusano, S.; Giacobello, F.; Tonella, S.; Oldani, C.; Aricò, A.S. Ce-radical Scavenger-Based Perfluorosulfonic Acid Aquivion® Membrane for Pressurised PEM Electrolysers. *Polymers* **2023**, *15*, 3906. [CrossRef] [PubMed]
48. Chu, Y.; Luo, E.; Wei, Y.; Zhu, S.; Wang, X.; Yang, L.; Gao, N.; Wang, Y.; Jiang, Z.; Liu, C.; et al. Dual single-atom catalyst design to build robust oxygen reduction electrode via free radical scavenging. *Chem Catal.* **2023**, *3*, 100532. [CrossRef]

49. Peera, S.G.; Koutavarapu, R.; Akula, S.; Asokan, A.; Moni, P.; Selvaraj, M.; Balamurugan, J.; Kim, S.O.; Liu, C.; Sahu, A.K. Carbon Nanofibers as Potential Catalyst Support for Fuel Cell Cathodes: A Review. *Energy Fuels* **2021**, *35*, 11761–11799. [CrossRef]
50. Chang, X.; Batchelor-McAuley, C.; Compton, R.G. Hydrogen peroxide reduction on single platinum nanoparticles. *Chem. Sci.* **2020**, *11*, 4416–4421. [CrossRef]